

Preparation of Ginger Straw based Porous Carbon using One-step Pyrolysis Process as Electrode Material for Supercapacitor

Jinxiao Li, Jiamin Wang, Kuihua Han*, Jianhui Qi, Ming Li, Zhaocai Teng, Meimei Wang

School of Energy and Power Engineering, Shandong University, 250061 Jinan, PR China

*E-mail: hankh@163.com

Received: 17 June 2019 / Accepted: 20 August 2019 / Published: 7 October 2019

Conventional preparation for porous carbon is expensive, complex, leading to a low yield. In this study, a one-step pyrolysis synthesis method without any chemical additive is designed based on the natural tubular structures and components (rich in potassium) of the ginger straw. The physicochemical and electrochemical performance of the product are studied, and the synthesis mechanism is discussed. Based on the excellent hierarchical porous structure, the specific capacitance can reach 274 F g^{-1} ($38.1 \mu\text{F cm}^{-1}$) @ 0.1 A g^{-1} , and the specific capacitance can retain 88% after 6000 cycles at the current density of 5 A g^{-1} . The maximum energy density and power density can be $34.06 \text{ W h kg}^{-1}$ and 4.35 kW kg^{-1} . This study provides a new perspective for designing preparation method based on the component and structure characteristics of the raw material, and provide a new perspective on the treatment of ginger straw waste.

Keywords: synthesis method; porous carbon; supercapacitor; electrochemical performance; biomass

1. INTRODUCTION

With the development of society and economy, energy demand is increasing worldwide. The traditional energy is facing serious situation due to its limited reserves, and the using process usually causes pollution to the environment. New energy resources, such as solar energy, wind energy, tidal energy, hydroenergy and geothermal energy[1, 2], are intermittent and instable[3], which bring challenges for the energy storage/conversion devices. Batteries, as one of the most popular energy storage device at present, has limited power density and poor cycle life[4], inducing a need for alternative devices with better performance. Supercapacitor, as a new type of energy storage device between traditional capacitor and battery, has many advantages such as: high power density, long cycle life, high charging/discharging efficiency, wide operating temperature range, high safety, and friendly to the environment. These peerless advantages make it a promising energy storage device in the future.

Supercapacitor can be generally divided into Electric Double Layer Capacitor (EDLC) and pseudocapacitor according to its energy storage mechanism[5]. The charge storage mechanism of EDLC is based on the electrostatic accumulation at the interface between electrode and electrolyte[6]. For pseudocapacitor, it is based on the reversible redox reactions on the surface of the electrode[7, 8]. Thus, it is obvious that the electrode material plays a very important role for each type of supercapacitor. For commercial EDLC, Porous Carbon (PC) is the most used electrode material because it has both high conductivity and large Specific Surface Area (SSA). High conductivity means low resistance, and large SSA represents large power storage capacity. The raw materials for preparing PCs can be generally divided into two types: biomass and minerals. Biomass-based PCs attract extensive attention in recent years[9, 10] because it is widely distributed, cheap, renewable and friendly to the environment [11].

China, as one of the major producer and exporter of Ginger Straw (GS), has over 2300 km² cultivated areas for it. The edible part of a ginger plant has equal weight to the rest part, so there is a considerable quantity of waste GS. However, the ginger plant has antibacterial components and antioxidant ingredients, which makes it hard to degrade. Besides, common ways to dispose GS wastes, like making into briquettes, converting into biogas, fermentation for ethanol, etc., have poor economic profits. Therefore, an efficient and practical way to treat these GS wastes is badly in need. Compared with the treatment above, converting GS into PC material for supercapacitor is a high-value utilization for GS and it is suitable for large-scale production.

Compared with other methods for preparing PC, the thermochemical method has simple processing steps and is easy to operate. Chemical activation method is one of the most popular ways among thermochemical methods by using different activating agents, such as KOH[12-16], H₃PO₄[17-19], ZnCl₂[20-22] and FeCl₃[23, 24]. Although the introduction of these chemical agents can create large SSA, it usually follows a series of problems, such as: causing serious corrosion to the equipment, bringing pollution to the environment, the product has a complex wash process, and the yield of the product is less than satisfactory. Recently, some researchers find that the self-contained alkali metal and alkali-earth metal elements in biomass can play an important role in the pyrolysis process[25, 26]. According to this theory, the raw materials rich in alkali/alkali-earth metal can realize self-activation during pyrolysis without adding an activating agent. Raymundo [27] carbonized the seaweed, which is rich in sodium alginate, and the product has the SSA for 1307 m² g⁻¹. Biswal [28] carbonized neem leaves rich in Ca and Mg, and the SSA of the product can reach 1230 m² g⁻¹. Zhang [29] produced lotus stem-based PC with a SSA of 1610 m² g⁻¹ by one-step pyrolysis, and they attributed the large SSA to the high content of K in the raw material. Usually, there is a higher content of alkali metal or alkali-earth metal elements in the stem than other parts of a plant for functional reasons. Therefore, GS should have a certain amount of alkali/alkali-earth metal, which means it is a potential precursor for self-activation. In this paper, GS was used as raw material, the one-step pyrolysis method was designed for preparing PCs, and the preparation mechanism was discussed. The structure, component and electrochemical performance of GS-based PC (GSPC) is studied.

2. EXPERIMENTAL

2.1. Fabrication of the PCs

The GS was washed and cut into 3 cm, put into an air-dry oven at 120 °C for 48 h. The dried GS was put into a pulverizer and smashed into powder. Then the powder was put into a tube furnace for pyrolysis with the heating rate of 5 °C min⁻¹. N₂ atmosphere was adopted, and the flow rate is 0.5 L min⁻¹. The pyrolysis temperature kept constant for 2 h after reaching the setting temperature. After cooling down to room temperature, the product was pickled by 1 M HCl and washed by deionized water until pH=7. The pyrolysis temperature ranges from 300 °C to 1000 °C. The final product was marked as GSPC-pyrolysis temperature in centigrade, e.g., GSPC-800.

2.2. Characterization of the GS and GSPC

X-Ray Fluorescence (XRF) analysis was used to identify the ash component for GS. Thermal analysis of the samples was carried out by using thermal gravimetric analyzer (TGA/SDTA851°, Mettler-Toledo). The thermal analysis was carried out under nitrogen atmosphere at a flow rate of 80 ml min⁻¹. The results of the thermal analysis can be reflected by Thermogravimetry (TG) curves and Derivative Thermogravimetry (DTG) curves. The carbon yield of GS can be calculated by this equation:

$$\varphi = \frac{m_2}{m_1} \times 100\% \quad (1)$$

where φ represents the carbon yield, m_1 (g) represents the mass of the GS and m_2 (g) represents the mass of GSPC. N₂ adsorption-desorption test was carried out at 77.4 K. The SSA was calculated by Barrett-Emmett-Teller (BET) method, the pore size and distribution of mesopores (2-50 nm) and micropores (<2 nm) were analyzed by Barrett-Joyner-Halenda (BJH) method and Horvath-Kawazoe (HK) method, respectively. The morphology and elemental composition of GS and GSPC were analyzed by Scanning Electron Microscopy (SEM) and Energy Dispersion Spectrum (EDS), respectively. The crystal structure of the samples was evaluated by X-Ray Diffraction (XRD), and the degree of graphitization of the samples was analyzed by Raman spectrum. The surface chemistry property of the carbon was analyzed by X-ray Photoelectron Spectroscopy (XPS).

2.3. Electrochemical measurement

GSPC, conductive graphite and polytetrafluoroethylene (PTFE) were mixed by the mass ratio of 8:1:1 in moderate absolute ethanol. The mixture was treated by ultrasonic dispersion and coated on a round nickel foam. After drying in a vacuum oven, the slice was pressed under 12 MPa for 1 min by a tablet machine. A sandwich-like button cell was assembled, and 6 M KOH was used as the electrolyte. The electrochemical performances of the samples were tested by an electrochemical workstation (CS310H, Wuhan Corrtest Instruments Corp., Ltd). The Galvanostatic Charge-Discharge (GCD) tests were carried out at the current density of 0.1 A g⁻¹-10 A g⁻¹, and the voltage window is 0-1 V. The specific capacitance can be calculated by this equation[30]:

$$C_M = \frac{4I\Delta t}{m\Delta V} \quad (2)$$

where C_M ($F g^{-1}$) represents the specific capacitance; I (mA) represents the discharging current; Δt (s) represents the discharging time; m (mg) represents the total mass of the PC on the electrode; ΔV (V) represents the potential difference during the discharging process. For practical application, the specific surface capacitance is more important, especially for small electronic equipment. The specific surface capacitance can be calculated by:

$$C_A = \frac{C_M}{S_{BET}} \quad (3)$$

where C_A ($\mu F cm^{-2}$) means the specific surface capacitance, and S_{BET} ($m^2 g^{-1}$) means the SSA calculated by BET method. The Cyclic Voltammetry (CV) curves were obtained in a potential range from 0-1 V by the scan rate varying from 5-200 mV. The Electrochemical Impedance Spectroscopy (EIS) analysis was performed at the frequency range between 0.01 Hz to 100 kHz with an amplitude of 5 mV. The energy density (E , $Wh kg^{-1}$) and power density (P , $W kg^{-1}$) can be calculated by the following equations:

$$E = \frac{C_M(\Delta V)^2}{8} \quad (4)$$

$$P = \frac{E}{\Delta t} \quad (5)$$

3. RESULTS AND DISCUSSION

3.1. The effect of preparation process

3.1.1. The effect of pyrolysis process

The pyrolysis process of biomass is mainly divided into three steps: the drying stage, the pyrolysis stage and the carbonization stage. For GS, the pyrolysis process can be analyzed from the TG/DTG curves. It can be seen from Fig.1(a) that both TG and DTG curves keep flat before 200°C, which corresponds to the drying stage. The reason for the weight loss at this stage is the evaporation of moisture. TG curve shows a sharp decrease from 200-350 °C, and DTG curve has an obvious inflection point at 290 °C. At that time, the weight loss ratio of the sample reaches 40%. This stage refers to the escape of volatile and the pyrolysis of cellulose. It can be seen that the decomposition rate at 300-550 °C is also fast, which can be attributed to the pyrolysis of hemicellulose and lignin. When the temperature exceeds 550 °C, the weight loss mainly depends on the process of slow pyrolysis of lignin and the formation of carbon. Fig.1(b) shows the relations between pyrolysis temperature and carbon yield, and the results are corresponding to Fig.1(a). When the temperature is lower than 400 °C, the carbon yield decreases sharply with the temperature increasing. When the temperature is between 400 °C-700 °C, the curve decreases slowly. When the temperature is higher than 700 °C, the carbon yield basically remain unchanged, and the carbon yield is around 30%. The carbon yield decreases again at 1000 °C because the temperature is higher than the ash fusion point, and some components in the ash can further decompose. The pyrolysis process can effectively remove moisture and the volatiles in the raw material with some changes happened in the structure and component.

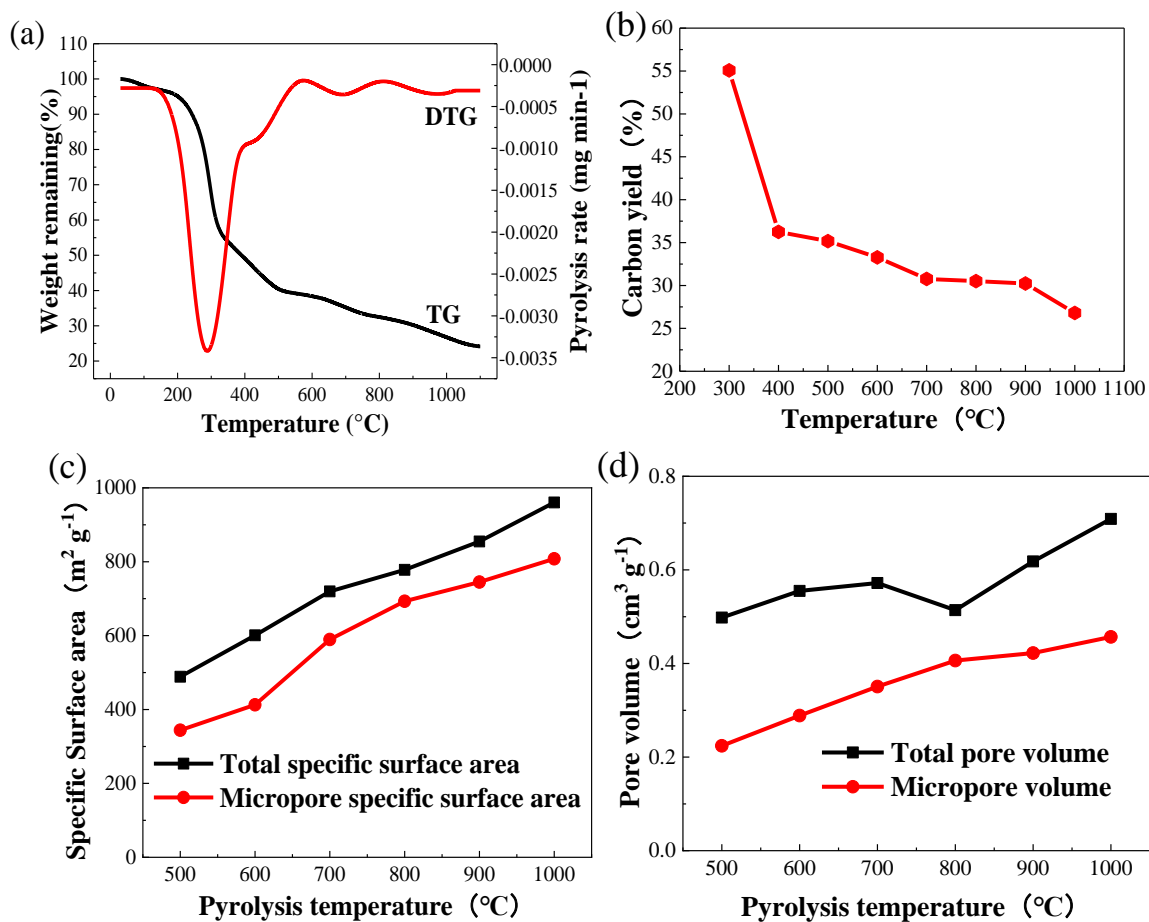


Figure 1. The effect of pyrolysis process (a) TG and DTG thermograms of GS (b) The yield of GSPC (c) The effect of different pyrolysis temperature on SSA (d) The effect of different pyrolysis temperature on pore volume

The pore structures of the samples can be analyzed based on the data of SSA and pore volume. The SSA of the samples prepared under 500°C is limited, therefore, their data are not shown in the further discussion. According to Fig.1(c) and Fig.1(d), the total SSA, the SSA for micropores, the total pore volume, and the pore volume for micropores are roughly increased with the increase of temperature. Combined with the analysis above, the moisture and the volatiles are escaped during the pyrolysis process, and many pores are formed at this time. The maximum of each parameter appears at 1000 °C. For some other biomass materials, the SSA of the carbonized product is very limited. The maximum SSA of GSPC-600 is 960 m² g⁻¹, which means obviously pore-forming process happens during the pyrolysis of GS. The SSA values of GSPCs are comparable to those biomass-based PC materials made by chemical activation, which means one-step pyrolysis synthesis is an ideal way to treat GS wastes and produce GSPC. What's more, the large SSA also means GSPCs have large space for charge storage. The maximum of total pore volume and the pore volume for micropores are 0.71 cm³ g⁻¹ and 0.46 cm³ g⁻¹, which means micropores account for a large proportion. It is widely accepted that micropores are the main structure to store charge, mesopores can transport the charge and macropores can store the electrolyte and act as the buffer zone[31, 32]. Therefore, high micropore content means GSPCs have

potential for electrode material for supercapacitor. The total pore volume shows a little decrease at 800 °C, and it can be explained by the ablated of some pores at high temperature.

The component of the samples can be analyzed based on the proximate analysis and ultimate analysis results, and GSPC-600 was chosen as the representative sample for the GSPCs. According to Tab.1, the GS is rich in carbon, which means it has the potential for high carbon yield. The contents of H and O in GSPC-600 decrease obviously with the release of the volatile, which causes the increase of the fixed carbon and the ash. More specific information about the content in the ash of GSPC-600 can be seen in Tab.2. It can be seen that potassium compound is the main constituent of the ash, and there are a small amount of Na, Mg and Ca. According to the former study, the alkali/alkali-earth metal elements can accelerate pyrolysis and create pores by self-activation effect [33, 34]. However, further analysis is still needed to explore whether the alkali/alkali-earth metal contributes to the formation of the pores.

Table 1. Proximate analysis and ultimate analysis of GS and GSPC-600

Sample	Proximate analysis (W/%, ad)				Ultimate analysis (W/%, ad)				
	M _{ad}	A _{ad}	V _{ad}	FC _{ad}	H _{ad}	C _{ad}	N _{ad}	S _{ad}	O _{ad}
GS	3.46	14.84	64.09	17.61	4.62	37.83	4.17	0.22	34.86
GSPC-600	3.21	35.63	11.34	49.82	1.58	50.36	3.06	0.34	5.82

Table 2. Ash component analysis of GS

Sample	Na ₂ O	MgO	Al ₂ O ₃	SiO ₂	P ₂ O ₅	SO ₃	Cl	K ₂ O	CaO	Fe ₂ O ₃	Other	Total
GS ash	0.69	3.59	0.26	2.45	3.01	2.28	2.2	73.7	5.81	0.34	5.64	100

3.1.2. The effect of acid pickling

The ash content in the electrode material should be low, because the existence of ash will reduce the electrical conductivity and block off the pores. According to Tab.1, the content of the ash is relatively high, and the main components in the ash are mostly alkali/alkali earth metal salts. Therefore, the acid pickling was necessary for removing these impurities. Fig.2 shows SEM results of GSPC before and after acid pickling. According to Fig.2(a), there are obvious impurities on the surface and inside the pores, and some pores are even blocked. After being pickled by HCl, the impurities are removed obviously and more pores are exposed (Fig.2(b)).

More information can be obtained from the EDS results. It can be seen from Fig.2(c) that there are a large amount of K and a certain amount of Mg and Cl in the GSPC, which is corresponding to the ash component (Tab.2). The XRD result shown in Fig.2(e) also confirms that the component of the ash is mainly potassium components, like K₂CO₃, KCO, K₂C₂O₆, and NaKCO₃. After acid pickling, the

impurities are effectively removed (Fig.2(d)), and only C and O can be observed. Compared to Fig.2(e), the peaks of impurities in Fig.2(f) are vanished, and broad peaks at $2\theta=22^\circ$ and $2\theta=44^\circ$ can be obviously observed, which means the dominant component of GSPC is amorphous carbon[28]. There are also sharp peaks near $2\theta=22^\circ$, which means the existence of certain ordered graphite structure. The existence of ordered graphite structure can improve the electrochemical performance by improving the electrical conductivity of the material.

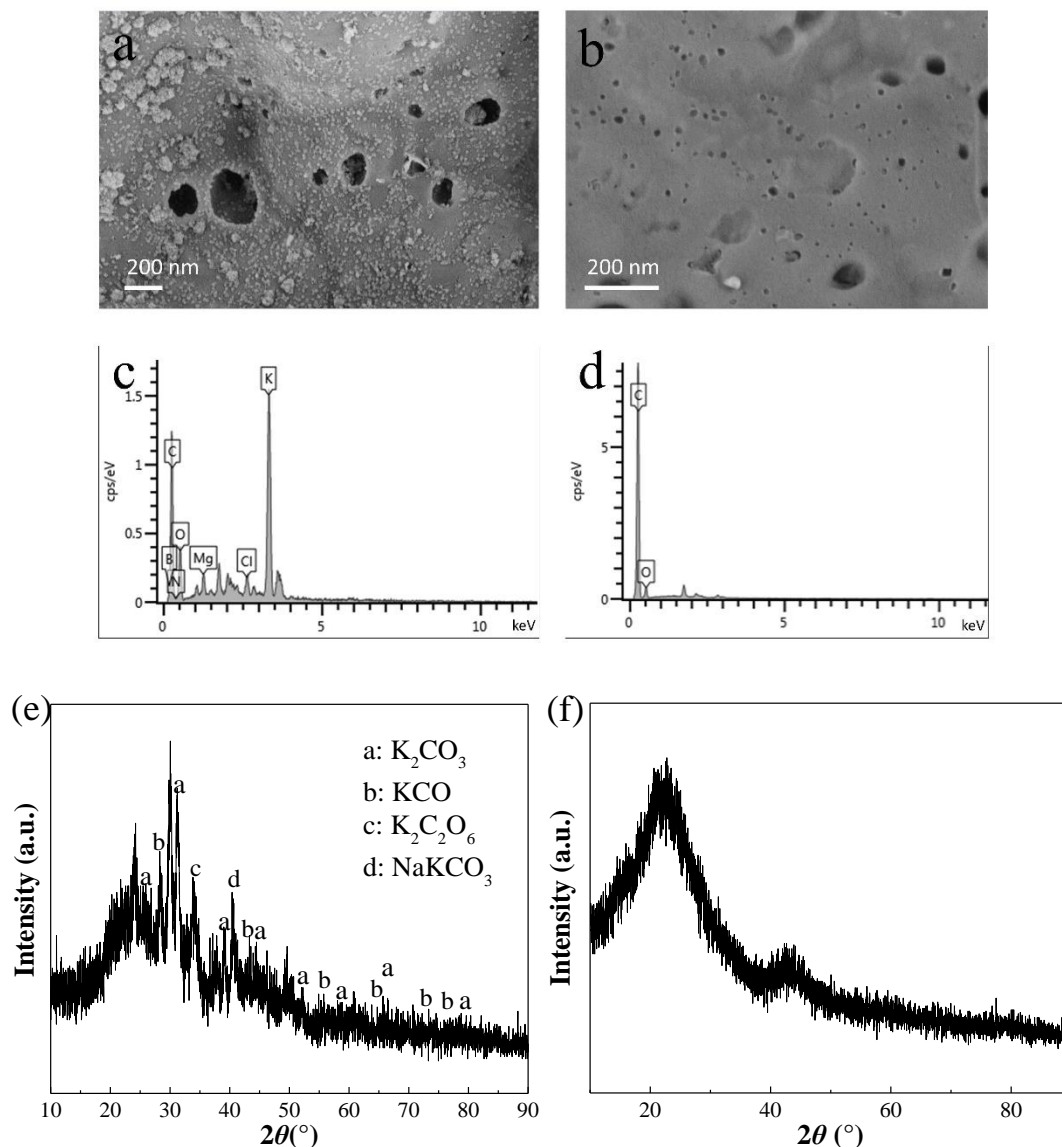


Figure 2. The effect of acid pickling on the GSPC-700 (a) SEM images of GSPC-700 before acid pickling (b) SEM images of GSPC-700 after acid pickling (c) EDS images of GSPC-700 before acid pickling (d) EDS images of GSPC-700 after acid pickling (e) XRD spectrum of GSPC-700 before acid pickling (f) XRD spectrum of GSPC-700 after acid pickling

3.2. Structure and morphology

The morphology of GS can be observed in Fig.3(a) and Fig.3(b). It can be seen that the GS have an obvious tubular structure, which is natural transport channels for ions. Initial pores on the surface of

GS is very limited, and they can hardly be observed. After pyrolysis (Fig.3(c) and Fig.3(d)), there are abundant circular pores appear on the surface, which is corresponding with the SSA data in Fig.1(c), indicating a huge potential for charge storage. All the N₂ adsorption-desorption curves of GSPCs in Fig.3(e) show obvious characteristics of IV type isothermal, which means multiple pore structures are existed in GSPCs[35]. When the relative pressure is low (<0.01), all the isothermals increase rapidly, which is nearly perpendicular to the horizontal axis. That means there are abundant micropores in the PCs[36, 37]. When the relative pressure is between 0.01-0.5, the adsorption curves tend to become flat, which can be attributed to the filling process of micropores.

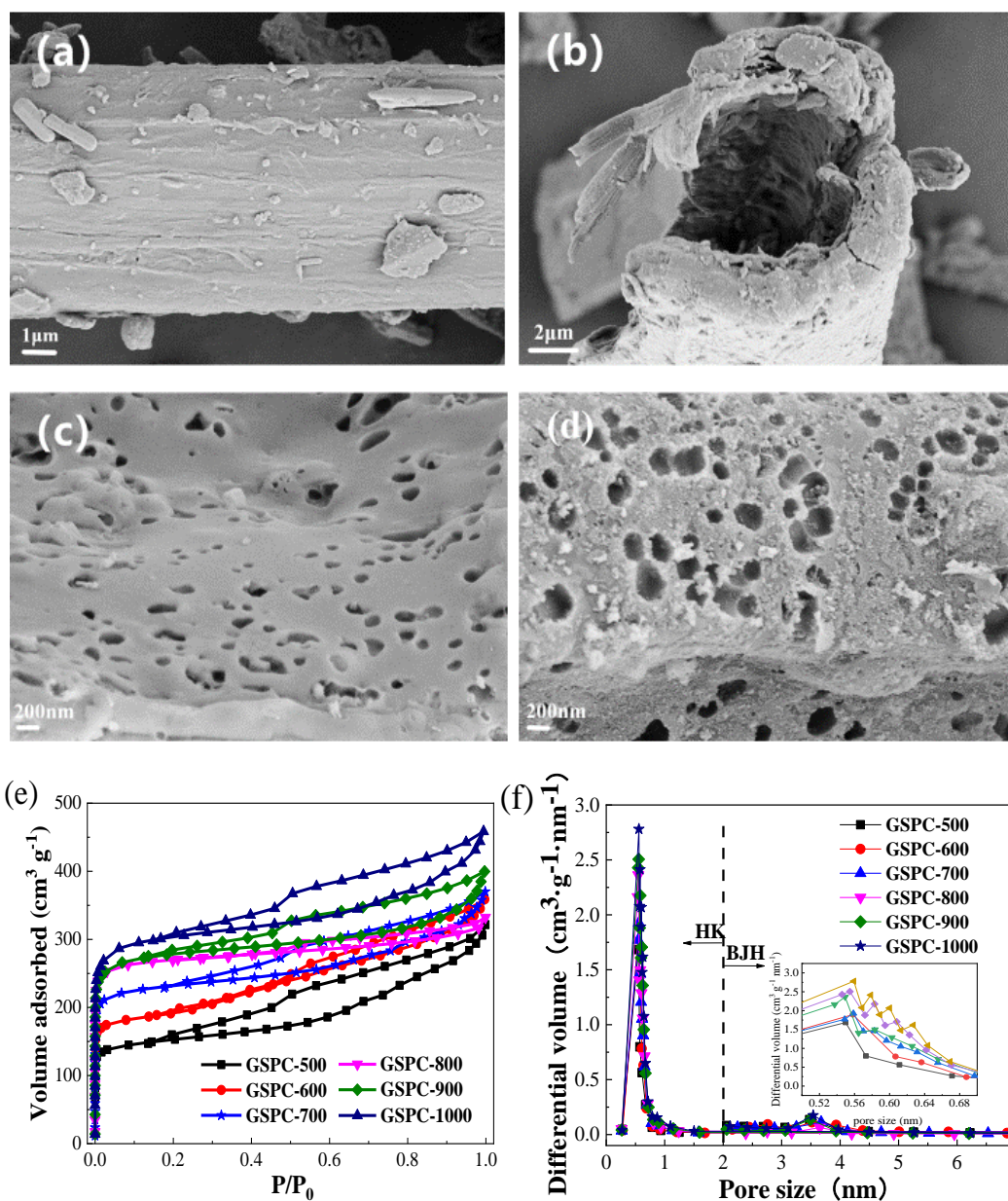


Figure 3. The morphology and structure of GS and GSPCs (a) The SEM images of GS (b) The SEM images of GS from the other side (c) The SEM images of GSPC-500 (d) The SEM images of GSPC-700 (e) The N₂ adsorption-desorption isotherms of GSPCs (f) The pore size distribution of GSPCs

When the relative pressure is 0.5-1, the hysteresis loops become obvious and the curves appear to be upward-sloping. It can be attributed to the condensation of the absorbent, which proves the existence of the mesopores in GSPC. For macropores(>50nm), it can be easily observed in the SEM images. Therefore, a conclusion can be drawn that GSPC has a hierarchical porous structure with macropores, mesopores, and micropores[38]. According to former studies, different pores have different functions during the energy-storage process, and the hierarchical structure can endow the GSPCs with good energy storage capacity.

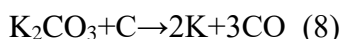
More specific information about pore diameter can be seen in Fig.3(f). For all the GSPCs, the pore diameters are mainly concentrated within 7 nm. The micropores are mainly concentrated between 0.5-0.7 nm, and the mesopores are mainly concentrated between 2-4 nm. The proportion of micropores are obviously higher than mesopores, which is corresponding to the analysis of Fig.3(e). According to former study, pores with diameter between 2-4 nm can provide channels for electrolyte ions, and pores with diameter between 0.4-1 nm can provide effective internal surface area for the adsorption of the charge[39, 40]. Based on the analysis above, the GSPCs are expected to have ideal electrochemical performance.

Combined with XRD analysis above, K_2CO_3 is one of the dominant component in the raw material. Take it as an example, and make the analysis of the pore-forming process of GSPC:

Under 333.6 °C, the K_2CO_3 will decompose by this equation:



According to the equation, the gaseous products will release at first, leaving pores at its original place. At higher temperature, the pyrolysis product of K_2CO_3 and unreacted K_2CO_3 can further react with carbide by the following equations:



According to these equations, pores are created with the consumption of carbon atoms, and abundant K is generated. With the temperature keeping rising and exceeding the boiling point of the potassium (762 °C), the gaseous potassium goes through the carbon layer and create new pores. However, potassium in the gas phase is very reactive, it can both create new pores and cause erosion to the previously formed pore structures. Some potassium salts are formed on the surface of the final product during the pyrolysis process. Combined with Fig.1(d), the total pore volume has an obvious decrease at 800 °C, it can be attributed to the erosion effect of the generated potassium vapor at that stage. At that time, some pore channels may be destroyed.

3.3. Electrochemical properties

The results of the GCD test, CV test, and EIS test are shown in Fig.4. According to Fig.4(a), all the GCD curves of GSPCs show good shapes of isosceles triangles, which means the GSPCs have good electrochemical reversibility[41]. GSPC-700 shows the longest charge-discharge time, which means it has the largest specific capacitance. It can be calculated by the eq.(2) that GSPC has the specific capacitance for 249 F g⁻¹ at the current density of 0.5 A g⁻¹.

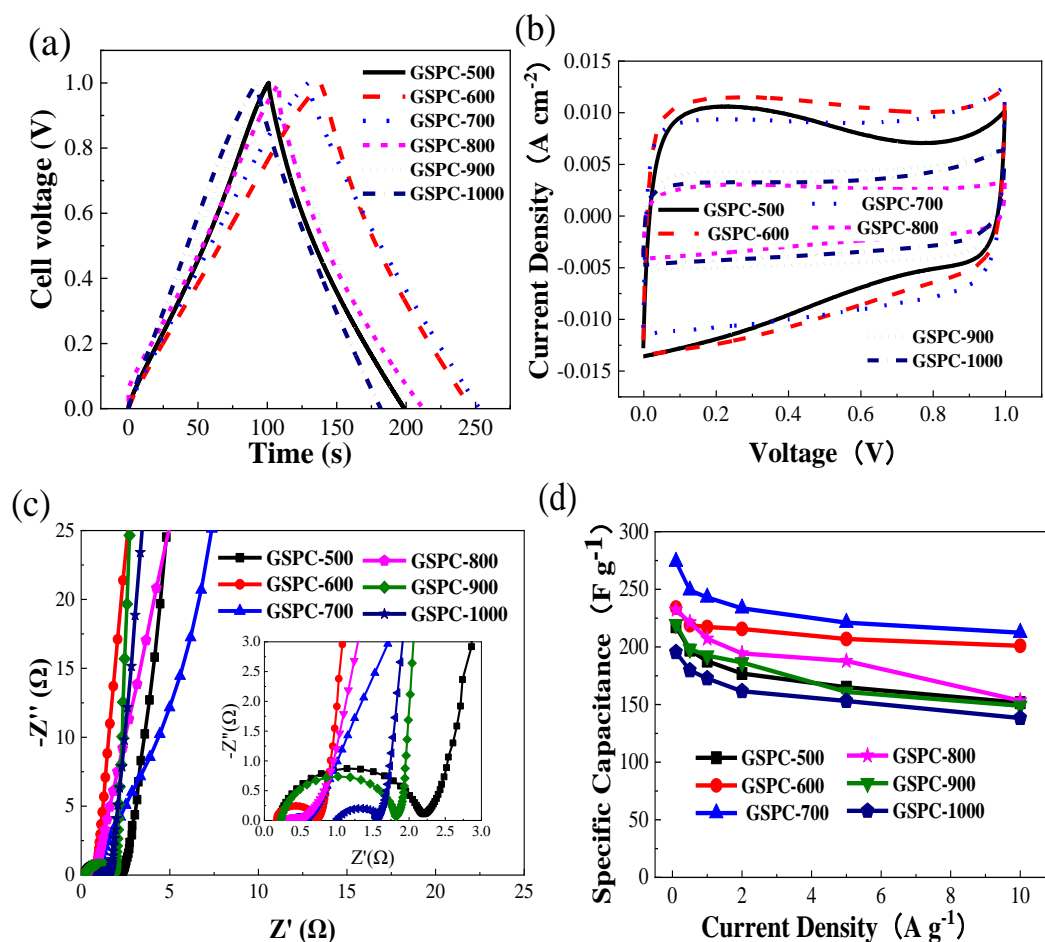


Figure 4. Electrochemical performance of GSPCs (a) GCD curves of GSPCs at the current density of 0.5 A g^{-1} (b) CV curves of GSPCs at the scan rate of 20 mV s^{-1} (c) The Nyquist plot of GSPCs (d) The rate performance of GSPCs at different current density

The CV curves of GSPCs exhibit approximate shapes of rectangular, which means all of them have good EDLC characters[42]. The bending of the rectangles can be attributed to the existence of functional groups, which can provide extra pseudocapacitance. The electrical resistance property of GSPCs can be analyzed by the Nyquist plots in Fig.4(c). The horizontal intercept of each curves stand for the Equivalent Series Resistance (ESR) of each sample[43, 44], and all the samples have ESR lower than 1Ω . The semicircle in the high frequency region of the Nyquist plot is related to the Charge-Transfer Resistance (R_{CT}) between the electrolyte and the electrode[45]. It can be seen that the GSPC-700 and GSPC-800 have smallest semicircular diameter, which means they have less resistance. In other words, their pore structures make the electrolyte ions easier to flow into the micropores. At low frequency region, all the curves behaves as the nearly vertical lines, which is corresponding to the results of Fig.4(b), representing the EDLC behavior. According to Fig.4(d), all the samples didn't show significant decline, which means these samples have good rate capability. Although the SSA keeps increasing with the temperature rising, GSPC-700 shows the largest specific capacitance at each current density. Combined with the analysis above, the gaseous potassium will destroy the pore structures and pore channels when the temperature exceeds $762 \text{ }^\circ\text{C}$. It can reach 274 F g^{-1} @ 0.1 A g^{-1} , and even 212 F g^{-1}

¹@10 A g⁻¹. It means there is only a 22.5% decrease when the current density increases 100 times. Except for the specific capacitance, specific surface capacitance is also an important factor for PC material as it can measure the efficiency of SSA to form the electric double layer. For GSPC-700, the value is 33.8 $\mu\text{F cm}^{-2}$.

Table 3. Several PCs derived from biomass for electrode material for supercapacitor

Ingredient	Activator	C_M (F g ⁻¹)	S_{BET} (m ² g ⁻¹)	C_A ($\mu\text{F cm}^{-2}$)	Test condition	Electrolyte	Ref
Shrimp shell	KOH	~295	1223	24.0	1 A g ⁻¹	6 M KOH	[46]
Rice husk	NaOH	210	1886	11.1	0.2 mA g ⁻¹	3 M KCl	[47]
Soybean root	KOH	~260	2143	12.1	1 A g ⁻¹	6 M KOH	[14]
Banana fibers	ZnCl ₂	74	1097	6.7	500 mA g ⁻¹	1 M Na ₂ SO ₄	[48]
Zymolignin	KOH	312	2218	14.1	1 A g ⁻¹	6 M KOH	[12]
Sugarcane bagasse	ZnCl ₂	300	1788	16.8	250 mA g ⁻¹	1 M H ₂ SO ₄	[49]
Cronstalk	KOH	230	1736	13.3	1 A g ⁻¹	6 M KOH	[16]
Argan seed shell	KOH/melamine	355	2062	17.2	2 mV s ⁻¹	6 M KOH	[50]
Pennisetum sinense	KOH	336	2532	13.3	1 A g ⁻¹	6 M KOH	[51]
Ginger straw	none	243	720	33.8	1 A g ⁻¹	6 M KOH	this work

Tab.3 shows the data of SSA, C_M and C_A of GSPC-700 and other biomass-derived PCs for further comparison. The SSA of PCs prepared by chemical activation is obviously larger than GSPC-700, but they don't have a distinct advantage in specific capacitance. According to the analysis above, although the content of alkali/alkali-earth metal elements in the GS is limited, the embedded elements can play the same role in the activation process. In addition, the surface capacitance of GSPC-700 is much higher, which means the SSA effectively provides the EDLC to a great extent. The theoretical specific surface capacitance of pure PC is 25 $\mu\text{F cm}^{-2}$, which is lower than GSPC-700, means part of the specific capacitance of GSPC is provided by pseudocapacitance.

For a conventional chemical activation, the dosage of chemical agent is usually several times more than the PC samples, which cause great damage to both the equipment and environment. In addition, the overuse activator will also lead to low carbon yield. But for the embedded alkali/alkali-earth metal, it has high efficiency to create pores. The GS has a natural tubular structure, which is good for the transportation for ions. The pores created based on the tubular structure can shorten the transport distance and increase the energy storage efficiency. Therefore, one-step pyrolysis based on the component and the structure features of GS is an excellent method to produce PC materials and treat GS waste.

3.4. Further analysis of GSPC-700

For most energy storage devices, the cycle performance, energy density and power density are very important factors. As analyzed above, GSPC-700 has the best specific capacitance. In this part, it

is chosen for further analyze. It can be seen from Fig.5(a) that after 6000 cycles, the capacitance retention can still be 88%, which means GSPC-700 has good stability in KOH electrolyte. The capacitance decay mainly happens at the first 3000 cycles, which can be attributed to the destruction of some functional groups. These functional groups can provide extra pseudocapacitance for supercapacitor by redox reactions. After 3000 cycles, the specific capacitance of GSPC-700 retains a relatively stable level because only physical energy storage happens at that stage.

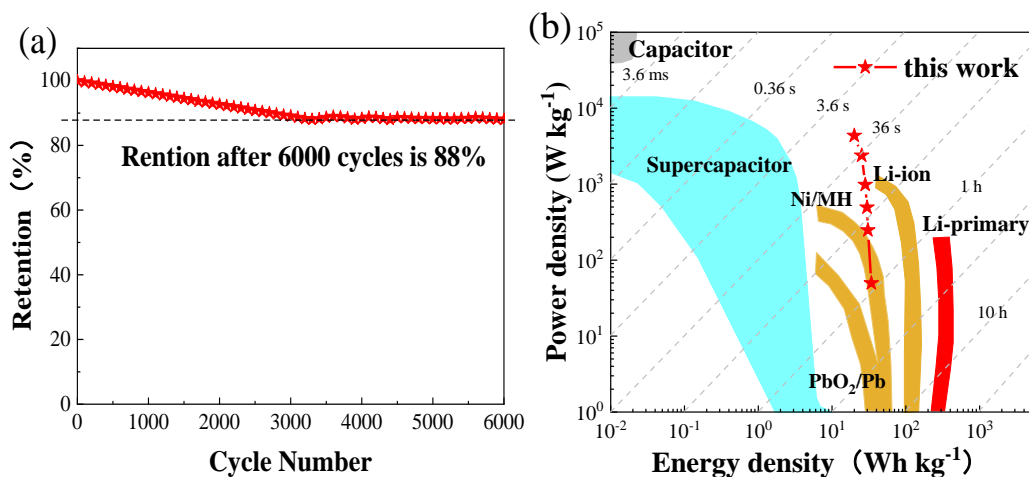
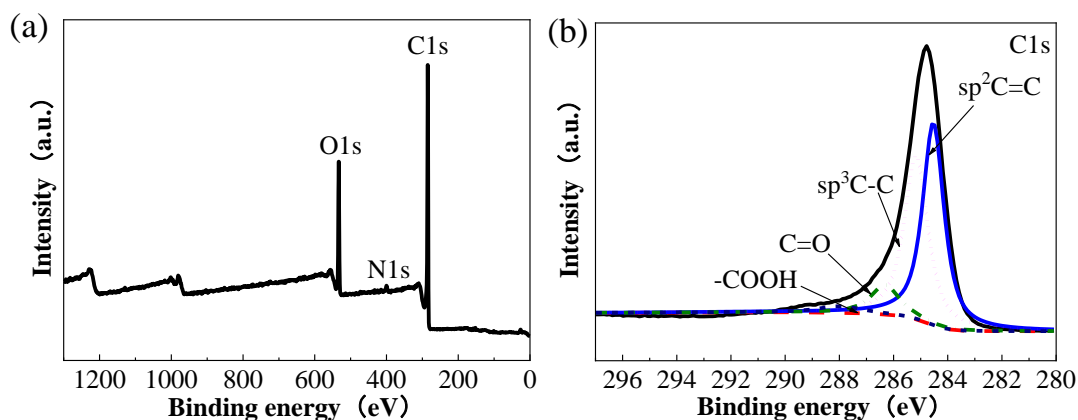


Figure 5. The cycle performance, energy density and power density of GSPC-700 (a) The capacitance retention of GSPC-7000 at the current density of 5 A g^{-1} after 6000 cycles (b) The energy density and power density of GSPC-700 and other energy storage devices

The main restriction on the applience of supercapacitor is the low energy density. At present, most of the supercapacitor has the energy density lower than 10 W h kg^{-1} . Fig.5(b) shows the comparison between GSPC-700 and other familiar energy storage devices about energy density and power density. It can be seen clearly that the GSPC-700 has obvious higher energy density than conventional supercapacitors, and have slightly better power density than conventional batteries. The maximum energy density of GSPC-700 can reach $34.06 \text{ W h kg}^{-1}$ @ 49.86 W kg^{-1} , and the maximum power density can reach 4.35 kW kg^{-1} @ $20.02 \text{ W h kg}^{-1}$.



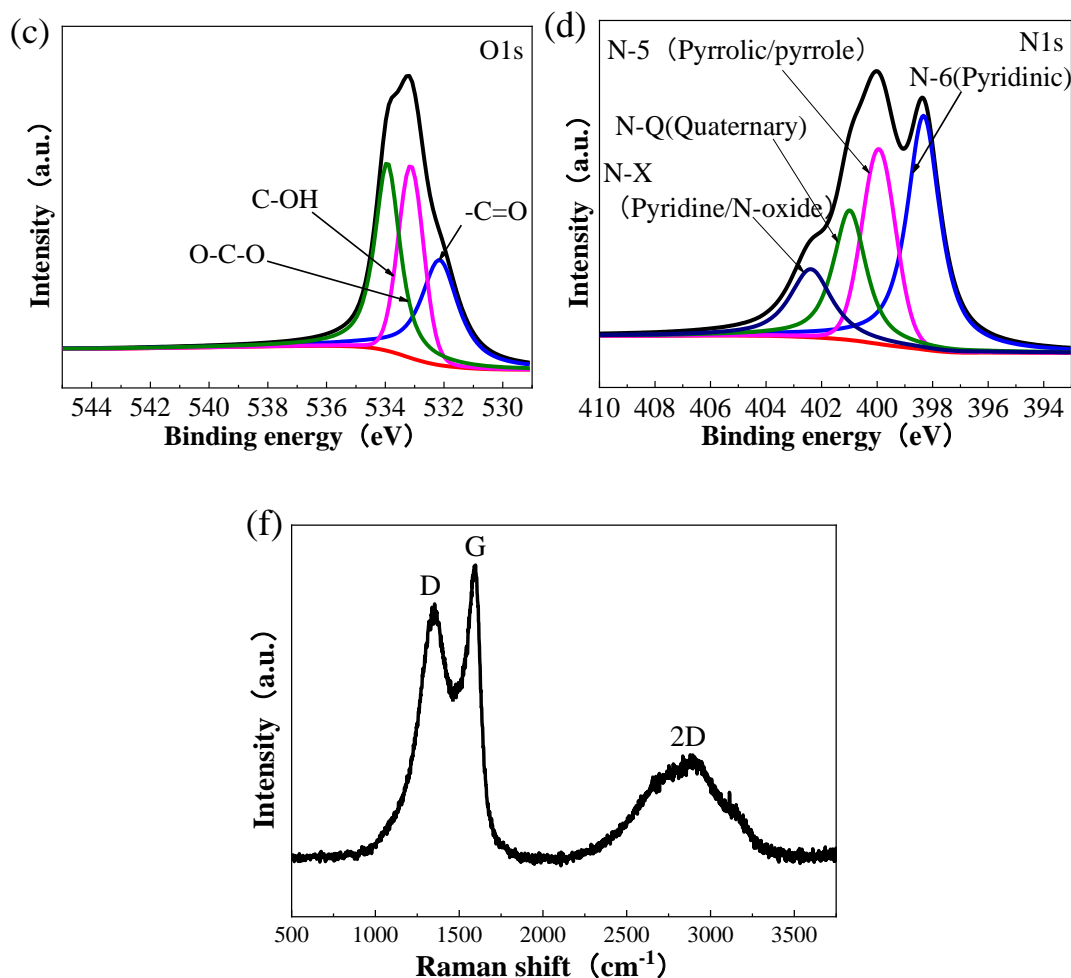


Figure 6. The XPS and Raman analysis of GSPC-700 (a) The XPS survey of GSPC-700 (b) High-resolution XPS analysis of the C1s peak of GSPC-700 (c) High-resolution XPS analysis of the O1s peak of GSPC-700 (d) High-resolution XPS analysis of the N1s peak of GSPC-700 (f) Raman spectrum of GSPC-700

The XPS results can reflect the chemical bond on the surface of the material. Fig.6 shows the XPS spectrum of GSPC-700 and the peak-differentiation-imitating analysis. The specific data of peak distribution can be seen in Tab.S1. According to Fig.6(a), the dominant elements of GSPC-700 is C, O and N, and the proportion of these three elements are 65.75%, 32.01% and 2.24%, respectively. This is corresponding to the EDS results above. The C1s spectrum (Fig.6(b)) can be deconvoluted into four peaks centered at 284.5 eV, 285.2 eV, 286.3 eV and 288.0 eV, assigned to C=C, C-C, C-O and –COOH[52]. The existence of C=C can effectively facilitate the charge transfer, and increases the conductivity[53]. The O1s spectrum (Fig.6(c)) can be deconvoluted into three peaks, located at 532.2 eV, 533.1 eV and 533.9 eV, which is corresponding to –C=O, C-OH and O-C-O, respectively[54]. The O1s spectrum (Fig.6(d)) can be deconvoluted into four peaks centered at 398.3 eV, 399.9 eV, 401.0 eV and 402.4 eV, corresponding to pyridinic nitrogen (N-6), pyrrolic/pyrrole nitrogen (N-5), quaternary nitrogen (N-Q), and pyridine/N-oxide (N-X)[55]. These oxygen or nitrogen-containing functional groups can provide additional pseudocapacitance for supercapacitor[46]. Meanwhile, these functional

groups can reduce the internal resistance by increase the accessible area for ions and improve the hydrophilicity of the material[56-58].

Raman spectrum is used for further analysis for the degree of graphitization of the GSPC-700. According to Fig.6(f), there are three obvious peaks including D band ($\sim 1350\text{ cm}^{-1}$), G band ($\sim 1580\text{ cm}^{-1}$) and 2D band ($\sim 2700\text{ cm}^{-1}$). The G band is attributed to the stretching vibration of the sp^2 hybrid surface, and the D band is assigned to the lattice imperfection of the carbon atom[59, 60]. The intensity ratio of G band and D band (I_G/I_D) can evaluate the degree of graphitization in a quantitative way. For GSPC-700, the value is 1.13, which is much higher than commercial activated carbon(0.52)[35, 61] and most of the studies [29, 35, 59, 61]. The 2D band means the existence of thin layer graphene, which can effectively improve the electrical conductivity[62]. In conclusion, the GSPC-700 exists in the form of amorphous carbon, and the comparatively high degree of graphitization can endows it with good electrical conductivity and low resistance.

3.5. Synthesis mechanism

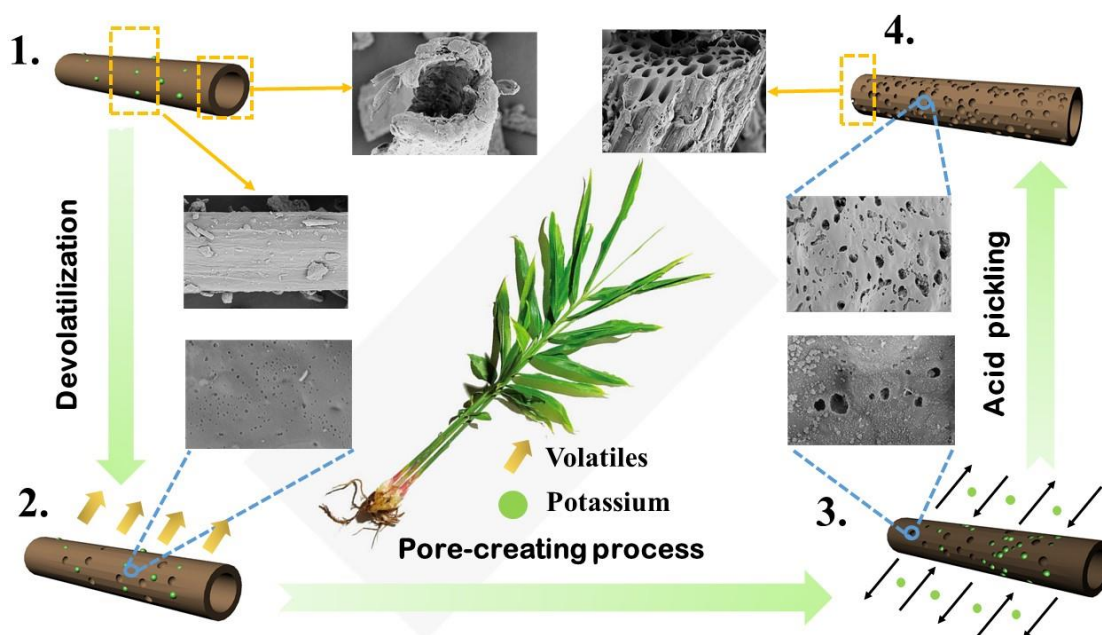


Figure 7. The synthesis mechanism of GSPC by one-step method

The synthesis mechanism of GSPC is summarized and shown in Fig.7. Based on the analysis above, GS has natural tubular structure embedded abundant alkali/alkali-earth metal elements, and potassium is the dominant elements. As shown in process 1., the tubular structure is natural transportation channels for ions. The alkali/alkali-earth elements can play a role as natural-embedded activators, and help to create pores during pyrolysis. When the temperature is low, the gaseous product releases first, leaving pores at its original place, which is corresponding to process 2.. At higher temperature, pores are created with the consumption of carbon atoms, and abundant K is generated. When the temperature exceeds the boiling point of the potassium, the gaseous potassium can create more

pores, which can be reflected by process **3**. After pyrolysis, there are obvious impurities on the surface of the material. It includes both the pyrolysis product and the reaction product. The use of HCl can effectively remove most of the impurities as shown in process **4**. Therefore, the pores are revealed and the pore channels are dredged. The tubular structure of the GS material can be well preserved after pyrolysis, and many pores are developed on its surface, which makes it a wonderful structure for the storage and transportation of charge. The synthesis mechanism helps to construct the hierarchical pore structures based on the natural tubular structure and high K content of GS is constructed, which makes the GSPC more suitable for energy storage.

4. CONCLUSION

Ginger straw-based porous carbon is successfully prepared by one-step pyrolysis based on its high content of K and natural tubular structure. The product has a high specific surface area ($960 \text{ m}^2 \text{ g}^{-1}$) with hierarchical pore structure and interconnected pore channels. The GSPC-700 show the best electrochemical performance, including high specific capacitance and high specific surface capacitance, good rate capability, long cycle life, good electric double-layer performance, small resistance, high power density and relatively high energy density. This paper provides a new perspective for the preparation of porous carbon for supercapacitor and a new handling method for ginger straw waste.

ACKNOWLEDGEMENT

The authors would like to acknowledge funding support by the Natural Science Foundation of Shandong, China (ZR2017MEE010), and the Fundamental Research Funds of Shandong University (2016JC005).

SUPPLEMENTARY MATERIAL

Table S1 Peak distribution of C 1s, O 1s, N 1s of GSPC-700

Peak	Binding energy (eV)	Assignment	Content(%)	Atom(%)
C 1s	284.5eV	sp ² C=C	46.3	65.7
	285.2eV	sp ³ C-C	41.4	
	286.3eV	C-O	9.1	
	288.0eV	-COOH	3.2	
O 1s	532.2 eV	-C=O	32.5	32.1
	533.1 eV	C-OH	29.8	
	533.9 eV	O-C-O	37.7	
N 1s	398.3 eV	N-6(Pyridinic)	39.8	2.2
	399.9 eV	N-5 (Pyrrolic/pyridone)	24.9	
	401.0 eV	N-Q(Quaternary)	21.0	
	402.4 eV	N-X (Pyridine/N-oxide)	14.3	

References

1. P. Simon, Y. Gogotsi, Materials for electrochemical capacitors, in: *Nanoscience And Technology: A Collection of Reviews from Nature Journals*, World Scientific, 2010, pp. 320-329.
2. S. Chu, A. Majumdar, *Nature*, 488 (2012) 294.
3. Z. Yang, J. Zhang, M.C. Kintner-Meyer, X. Lu, D. Choi, J.P. Lemmon, J. Liu, *Chem. Rev.*, 111 (2011) 3577-3613.
4. S. Chun, in, Carnegie Mellon University, 2011.
5. X. Wang, W. Zhang, M. Chen, X. Zhou, *Polymers*, 10 (2018) 1306.
6. Y. Zhang, X. Liu, S. Wang, L. Li, S. Dou, *Adv. Energy Mater.*, 7 (2017).
7. Y. Huang, M. Zhu, Y. Huang, H. Li, Z. Pei, Q. Xue, Z. Liao, Z. Wang, C. Zhi, *J. Mater. Chem. A*, 4 (2016) 4580-4586.
8. X. Chen, H. Wang, H. Yi, X. Wang, X. Yan, Z. Guo, *J. Phys. Chem. C*, 118 (2014) 8262-8270.
9. J. Deng, M. Li, Y. Wang, *Green Chem.*, 18 (2016) 4824-4854.
10. J. Wang, P. Nie, B. Ding, S. Dong, X. Hao, H. Dou, X. Zhang, *J. Mater. Chem. A*, 5 (2017) 2411-2428.
11. S. Imtiaz, J. Zhang, Z.A. Zafar, S. Ji, T. Huang, J.A. Anderson, Z. Zhang, Y. Huang, *Sci. China Mater.*, 59 (2016) 389-407.
12. L. Zhang, T. You, T. Zhou, X. Zhou, F. Xu, *ACS Appl. Mater. Interfaces*, 8 (2016) 13918-13925.
13. P. Cheng, T. Li, H. Yu, L. Zhi, Z. Liu, Z. Lei, *J. Phys. Chem. C*, 120 (2016) 2079-2086.
14. N. Guo, M. Li, Y. Wang, X. Sun, F. Wang, R. Yang, *ACS Appl. Mater. Interfaces*, 8 (2016) 33626-33634.
15. Y. Cai, Y. Luo, Y. Xiao, X. Zhao, Y. Liang, H. Hu, H. Dong, L. Sun, Y. Liu, M. Zheng, *ACS Appl. Mater. Interfaces*, 8 (2016) 33060-33071.
16. H. Yu, W. Zhang, T. Li, L. Zhi, L. Dang, Z. Liu, Z. Lei, *RSC Adv.*, 7 (2017) 1067-1074.
17. J. Qu, C. Geng, S. Lv, G. Shao, S. Ma, M. Wu, *Electrochim. Acta*, 176 (2015) 982-988.
18. C. Huang, A.M. Puziy, T. Sun, O.I. Poddubnaya, F. Suárez-García, J.M. Tascón, D. Hulicova-Jurcakova, *Electrochim. Acta*, 137 (2014) 219-227.
19. J. Li, K. Han, S. Li, *J. Mater. Sci.: Mater. Electron.*, 29 (2018) 8480-8491.
20. W. Liu, H. Jiang, H. Yu, *Chem. Rev.*, 115 (2015) 12251-12285.
21. X. He, P. Ling, M. Yu, X. Wang, X. Zhang, M. Zheng, *Electrochim. Acta*, 105 (2013) 635-641.
22. M. Wu, P. Li, Y. Li, J. Liu, Y. Wang, *RSC Adv.*, 5 (2015) 16575-16581.
23. T.E. Rufford, D. Hulicova-Jurcakova, Z. Zhu, G.Q. Lu, *J. Mater. Res.*, 25 (2010) 1451-1459.
24. A. Elmouwahidi, E. Bailón-García, A.F. Pérez-Cadenas, F.J. Maldonado-Hódar, F. Carrasco-Marín, *Electrochim. Acta*, 229 (2017) 219-228.
25. Y. Le Brech, T. Ghislain, S. Leclerc, M. Bouroukba, L. Delmotte, N. Brosse, C. Snape, P. Chaimbault, A. Dufour, *ChemSusChem*, 9 (2016) 863-872.
26. K. Haddad, M. Jeguirim, S. Jellali, C. Guizani, L. Delmotte, S. Bennici, L. Limousy, *Energy*, 134 (2017) 10-23.
27. E. Raymundo-Piñero, M. Cadek, F. Béguin, *Adv. Funct. Mater.*, 19 (2009) 1032-1039.
28. M. Biswal, A. Banerjee, M. Deo, S. Ogale, *Energy Environ. Sci.*, 6 (2013) 1249-1259.
29. Y. Zhang, S. Liu, X. Zheng, X. Wang, Y. Xu, H. Tang, F. Kang, Q.H. Yang, J. Luo, *Adv. Funct. Mater.*, 27 (2017).
30. D. Kang, Q. Liu, J. Gu, Y. Su, W. Zhang, D. Zhang, *ACS nano*, 9 (2015) 11225-11233.
31. K. Naoi, P. Simon, *Electrochem. Soc. Interface*, 17 (2008).
32. L. Zhang, L. Liu, M. Liu, Y. Yu, Z. Hu, B. Liu, H. Lv, A. Chen, *J. Alloys Compd.*, 778 (2019) 294-301.
33. P.T. Williams, P.A. Horne, *Renewable Energy*, 4 (1994) 1-13.
34. K. Davidsson, J. Korsgren, J. Pettersson, U. Jäglid, *Fuel*, 81 (2002) 137-142.

35. H. Wang, Z. Xu, A. Kohandehghan, Z. Li, K. Cui, X. Tan, T.J. Stephenson, C.K. King'Ondu, C.M. Holt, B.C. Olsen, *Acs Nano*, 7 (2013) 5131-5141.
36. M.A. Habila, Z.A. ALOthman, S.A. Al-Tamrah, A.A. Ghafar, M. Soylak, *J. Ind. Eng. Chem.*, 32 (2015) 336-344.
37. A. Gomis-Berenguer, L.F. Velasco, I. Velo-Gala, C.O. Ania, *J. Colloid Interface Sci.*, 490 (2017) 879-901.
38. X. Yang, H. Ma, G. Zhang, *Langmuir*, 33 (2017) 3975-3981.
39. J. Chmiola, G. Yushin, R. Dash, Y. Gogotsi, *J. Power Sources*, 158 (2006) 765-772.
40. J. Huang, B.G. Sumpter, V. Meunier, *Chemistry—A European Journal*, 14 (2008) 6614-6626.
41. H. Sun, W. He, C. Zong, L. Lu, *ACS Appl. Mater. Interfaces*, 5 (2013) 2261-2268.
42. C. Long, L. Jiang, X. Wu, Y. Jiang, D. Yang, C. Wang, T. Wei, Z. Fan, *Carbon*, 93 (2015) 412-420.
43. L. Wei, M. Sevilla, A.B. Fuertes, R. Mokaya, G. Yushin, *Adv. Funct. Mater.*, 22 (2012) 827-834.
44. C. Ramirez-Castro, C. Schütter, S. Passerini, A. Balducci, *Electrochim. Acta*, 206 (2016) 452-457.
45. X. Yang, J. Zhu, L. Qiu, D. Li, *Adv. Mater.*, 23 (2011) 2833-2838.
46. W. Yang, Z. Du, Z. Ma, G. Wang, H. Bai, G. Shao, *RSC Adv.*, 6 (2016) 3942-3950.
47. Y. Guo, J. Qi, Y. Jiang, S. Yang, Z. Wang, H. Xu, *Mater. Chem. Phys.*, 80 (2003) 704-709.
48. V. Subramanian, C. Luo, A.M. Stephan, K. Nahm, S. Thomas, B. Wei, *J. Phys. Chem. C*, 111 (2007) 7527-7531.
49. T.E. Rufford, D. Hulicova-Jurcakova, K. Khosla, Z. Zhu, G.Q. Lu, *J. Power Sources*, 195 (2010) 912-918.
50. A. Elmouwahidi, Z. Zapata-Benabithé, F. Carrasco-Marín, C. Moreno-Castilla, *Bioresour. Technol.*, 111 (2012) 185-190.
51. Y. Liu, B. Huang, X. Lin, Z. Xie, *J. Mater. Chem. A*, 5 (2017) 13009-13018.
52. D. He, J. Niu, M. Dou, J. Ji, Y. Huang, F. Wang, *Electrochim. Acta*, 238 (2017) 310-318.
53. M. Mosher, in, ACS Publications, 1992.
54. H. Xu, S. Yuan, Z. Wang, Y. Zhao, J. Fang, L. Shi, *RSC Advances*, 4 (2014) 8472-8480.
55. Y. Li, Z. Wang, L. Li, S. Peng, L. Zhang, M. Srinivasan, S. Ramakrishna, *Carbon*, 99 (2016) 556-563.
56. Y. Huang, L. Peng, Y. Liu, G. Zhao, J.Y. Chen, G. Yu, *ACS Appl. Mater. Interfaces*, 8 (2016) 15205-15215.
57. N. Guo, M. Li, X. Sun, F. Wang, R. Yang, *Green Chem.*, 19 (2017) 2595-2602.
58. J. Bao, C. Liang, H. Lu, H. Lin, Z. Shi, S. Feng, Q. Bu, *Energy*, 155 (2018) 899-908.
59. C. Chen, D. Yu, G. Zhao, B. Du, W. Tang, L. Sun, Y. Sun, F. Besenbacher, M. Yu, *Nano Energy*, 27 (2016) 377-389.
60. M.S. Liu, L.A. Bursill, S. Prawer, R. Beserman, *Phys. Rev. B*, 61 (2000) 3391.
61. W. Tian, Q. Gao, Y. Tan, K. Yang, L. Zhu, C. Yang, H. Zhang, *J. Mater. Chem. A*, 3 (2015) 5656-5664.
62. C. Liu, W. Chen, M. Li, S. Hong, W. Li, M. Pan, Q. Wu, C. Mei, *RSC Advances*, 9 (2019) 19441-19449.